

SNS junctions in nanowires with spin-orbit coupling: role of confinement and helicity on the sub-gap spectrum

Jorge Cayao¹, Elsa Prada², Pablo San-Jose¹ and Ramón Aguado¹

¹*Instituto de Ciencia de Materiales de Madrid (ICMM-CSIC), Cantoblanco, 28049 Madrid, Spain*

²*Universidad Autónoma de Madrid, Cantoblanco, 28049 Madrid, Spain*

(Dated: April 19, 2022)

We study normal transport and the sub-gap spectrum of superconductor-normal-superconductor (SNS) junctions made of semiconducting nanowires with strong Rashba spin-orbit coupling. We focus, in particular, on the role of confinement effects in long ballistic junctions. In the normal regime, scattering at the two contacts gives rise to two distinct features in conductance, Fabry-Perot resonances and Fano dips. The latter arise in the presence of a strong Zeeman field B that removes a spin sector in the leads (*helical* leads), but not in the central region. Conversely, a helical central region between non-helical leads exhibits helical gaps of half-quantum conductance, with superimposed helical Fabry-Perot oscillations. These normal features translate into distinct subgap states when the leads become superconducting. In particular, Fabry-Perot resonances within the helical gap become parity-protected zero-energy states (parity crossings), well below the critical field B_c at which the superconducting leads become topological. As a function of Zeeman field or Fermi energy, these zero-modes oscillate around zero energy, forming characteristic loops, which evolve continuously into Majorana bound states as B exceeds B_c . The relation with the physics of parity crossings of Yu-Shiba-Rusinov bound states is discussed.

I. INTRODUCTION

Majorana fermions, particles that are their own antiparticles, have been the subject of intense research over the past decades in the context of particle physics and cosmology^{1,2}. During the last few years, this interest extended to the condensed matter arena where Majorana fermions are intensely studied nowadays^{3,4}. This state of affairs has been driven by the key observation that emergent quasiparticles in superconductors can be described as Majorana fermions⁵. This, together with the recent advances in the field of topological materials^{6,7}, has spurred an intense search for condensed matter realizations of Majorana fermions. Most of these realizations focus on zero-energy modes inside the gap of topological superconductors. These zero modes are Majoranas from the point of view of particle-antiparticle conjugation, but they do not obey fermionic exchange statistics⁸. Thus, instead of Majorana fermions, they are now more precisely referred to as Majorana bound states (MBSs) or Majorana zero modes.⁹

Early proposals suggested that MBSs can emerge in exotic superconductors, such as p-wave, since they realize topological phases that support edge excitations with Majorana fermion character¹⁰⁻¹⁵. Even though p-wave pairing is not robust against disorder and thus scarce in nature, one can engineer systems to mimic such non trivial superconductivity. These are based on the proximity effect between a conventional s-wave superconductor and a topological insulator¹⁶, or a semiconductor nanowire (NW) with strong spin-orbit (SO) coupling¹⁷⁻²¹. For the latter case it has been shown^{20,21} that if an external Zeeman field B , orthogonal to the SO axis, exceeds a critical value $B_c \equiv \sqrt{\mu^2 + \Delta^2}$, where μ is the Fermi energy and Δ the induced s-wave pairing, zero energy MBSs emerge at the nanowire ends signaling a topologically non-trivial

phase.

Unfortunately, the outcome of the simplest detection protocol for MBSs in NW devices²²⁻²⁴, detection of subgap zero modes through zero-bias anomalies in transport²⁵⁻³⁰, can be obscured, or even mimicked, by other effects³¹⁻³⁸. As a result, there is no clear consensus yet on whether MBSs have been observed or not in NWs³⁹.

Thus, the time seems right to move beyond zero-bias anomaly experiments and study more complex geometries such as Superconductor-Normal-Superconductor (SNS) junctions^{40,41}. This geometry has a number of advantages including the possibility of studying supercurrents⁴²⁻⁴⁶, or direct spectroscopy of Andreev bound states (ABS)^{30,47-54}. As we shall discuss, this latter technique can be used, in principle, to directly monitor the detailed evolution from the trivial to the nontrivial regime. Previous papers have mostly focused on short junctions^{40,55,56} while detailed studies of ABS in other relevant geometries, including long and intermediate-length junctions, remain largely unaddressed. In particular, the role of Fabry-Perot resonances occurring in normal transport as the middle NW finite-length section of the junction is depleted has never been studied to the best of our knowledge. In this work we fill this void and present detailed calculations of the normal conductance and Andreev spectra in such geometries. We emphasize here that all nanowire experiments should ideally belong to the category studied here, as confinement effects should be present when a ballistic quasi-one dimensional conductor is contacted between electrodes, especially when the normal part of the NW (in our geometry, the part not directly in contact with electrodes) is gated.

In the first half of this work, we discuss normal transport across a finite length ballistic NW. We show how bandstructure details in the presence of strong Rashba

SO coupling and Zeeman fields may dominate transport, and give rise to distinct features associated to helical phases (defined by singly-degenerate subbands at the Fermi level with spin locked to momentum) known as helical gaps (Fig. 1). Likewise, finite contact resistance induces confinement resonances in conductance as quasibound states develop in the NW. In the simplest case of non-interacting electrons⁵⁷, we find that confinement generates two types of resonances: Fabry-Perot resonances and helical Fano dips. Fabry-Perot resonances for a spinful mode⁵⁸ will give conductance oscillations with a ceiling of $2e^2/h$, unless the central NW is depleted into its helical regime, in which case one may observe *helical* Fabry-Perot resonances with a half-quantum e^2/h ceiling. For long enough junctions, many helical Fabry-Perot resonances may occur. We discuss that, while confinement effects may mask the helical gap, the characteristic reentrance of helical Fabry-Perot resonances with Zeeman field or gate voltage contains valuable information about non-trivial helical transport through the NW. The second kind of resonances are sharp Fano dips when the central section of the NW is gated to form a quantum well (non-helical) and the NW sections below the contacts (the leads) are helical. Therefore, both types of resonant features in normal transport may signal the helical regime in different sections (central or below the contacts) of the NW. In the presence of superconducting leads, the two lead to distinct effects.

In the second half of this work we consider the connection of this phenomenology to transport in the superconducting regime. Each helical Fano dip in the normal phase translates, in an SNS geometry, into a single subgap state that crosses zero energy as a function of external parameters (Fermi energy or Zeeman field). Such a crossing is often known as a *parity crossing*, since it is protected by conservation of number parity in the junction. As we discuss, these parity crossings are made possible by the nontrivial topology in the underlying effective p-wave superconductor for $B > B_c$. Similar bound states originated from nonmagnetic impurities in topological superconductors and superfluids have been recently discussed in Refs. 59 and 60 and can be considered the p-wave counterparts of Yu-Shiba-Rusinov bound states⁶¹⁻⁶⁴ in standard s-wave superconductors with magnetic impurities. A more direct analogy with standard Yu-Shiba-Rusinov magnetic bound states actually applies in the non-topological phase $B < B_c$. In this situation, helical Fabry-Perot resonances in normal conductance translate, in the superconducting regime, into loops around zero energy in the ABS spectrum as a function of external parameters. For long junctions, many of these loops are visible, each separated by a parity crossing at zero energy. As a result, the $B < B_c$ subgap spectrum contains near-zero energy subgap states that oscillate as a function of Fermi energy or Zeeman field when the N region of the junction is helical. Interestingly, we find that these oscillating near-zero subgap states in the trivial regime are smoothly connected to MBS when Zeeman is increased

beyond B_c .

This paper is organized as follows. In section II we describe the Hamiltonian model employed in our work. Section III focuses on the normal conductance and how the two types of resonances, helical Fabry-Perot and helical Fano dips, appear in the system. The rest of the paper is devoted to analysing the consequences of these resonant levels in the sub-gap spectrum in the superconducting regime. After a brief discussion on how the SNS junction is modeled, as well as a discussion about the relevant length scales of the problem, section IV presents a systematic study of the subgap spectrum of SNS junctions, including its dependence on the superconducting phase difference across the junction, φ . We discuss in detail how the presence of confined levels within the central region affect the ABS and lead to parity crossings in the topological phase. The dependence of the ABS on phase difference, Fermi energy of the normal region and Zeeman field is discussed for both short and long junctions in subsections IV B and IV C, respectively. Our conclusions are presented in Section V. In appendix A we describe in detail how we model SNS junctions by using a tight-binding version of the model presented in Section II. Appendix B discusses an effective model that fully explains the phenomenology behind helical Fano resonances.

II. NANOWIRE MODEL

We present the model for a nanowire with Rashba SOC and in the presence of an external Zeeman. We restrict ourselves to the strictly one dimensional (single-mode) case for simplicity. Generalisations to multimode nanowires are relatively straightforward. The model Hamiltonian reads

$$H_0 = \frac{p^2}{2m^*} - \mu - \frac{\alpha_R}{\hbar} \sigma_y p + B \sigma_x, \quad (1)$$

Here, p is the momentum operator, m^* is the effective electron mass, α_R the Rashba SOC strength, μ the Fermi energy and σ_i the spin Pauli matrices. An external magnetic field \mathcal{B} along the wire produces a Zeeman splitting $B = g\mu_B\mathcal{B}/2$, where μ_B is the Bohr magneton and g the wire g -factor. The Rashba coupling defines a typical length, the spin-orbit length $l_{SO} \equiv \hbar/\sqrt{2m^*E_{SO}}$, with the spin-orbit energy defined as $E_{SO} = \frac{1}{2}\alpha_R^2 m^*/\hbar^2$. For typical InSb values $m^* = 0.015m_e$, with m_e the electron mass and $\alpha_R = 0.2$ eV Å, the spin-orbit energy is $E_{SO} \approx 50\mu\text{eV}$ which gives SO lengths of the order of $l_{SO} \approx 200\text{nm}$.

Note that the Rashba and Zeeman fields in Eq.(1) are perpendicular. As a result, the two spinful bands (shifted by SO) become mixed by the Zeeman term and the zero-field crossing point at zero momentum becomes an anticrossing of size $2B$. When the chemical potential lies within this anticrossing gap, the system has two Fermi points, as opposed to four Fermi points for μ above or below this gap. This window is a *helical* gap, since

the two fermi points correspond to counter propagating states with different spins (the spin projection is locked to momentum)⁶⁵, see inset in Fig. 1.

III. THE NORMAL CONDUCTANCE

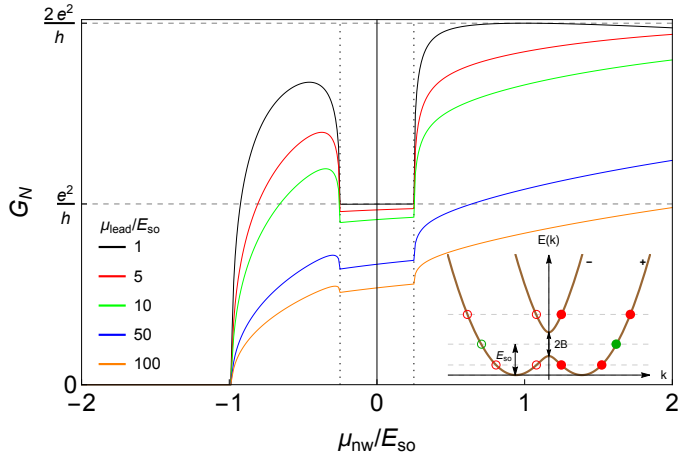


FIG. 1. (Color online) Normal conductance G_N as a function of the Fermi energy μ_{nw} in the left lead for a semi-infinite NW-N junction. Parameters: $\alpha_R = 20 \text{ meV nm}$ (which corresponds to $E_{SO} = 0.05 \text{ meV}$) and $B = 0.0125 \text{ meV}$. Different curves show how $G_N(\mu_{nw})$ evolves for increasing Fermi energy μ_{lead} in the right lead. The inset shows the dispersion relation for a Rashba NW in the presence of a transverse B field. Within the gap there is only one right mover per energy (green filled circle), while outside the gap there are two (red filled circles). This gives rise to the reentrant behavior of conductance, from $\sim 2e^2/h$ to e^2/h and back to $2e^2/h$, as a function of Fermi energy in the main panel. The spin of the counter propagating states (open circles) is opposite to the propagating ones (filled circles), hence the name helical.

Before discussing the sub-gap Andreev spectrum of a NW coupled to superconducting leads, we characterize the normal regime in the presence of a Zeeman field. We are interested in particular in the normal conductance G_N as the Fermi energy (μ_{nw}) in the middle section of the NW (length L_N) varies with respect to the one in the left and right leads μ_{leads} . Such situation models a NW contacted between normal electrodes and with a Fermi energy tuned by a central gate, see e. g. Ref. 29. For simplicity in the discussion, we model the gate-induced electrostatic potential with an abrupt profile (the role of smooth gate potentials has been recently discussed in Ref. 66).

For computations purposes we discretize Eq. (1) into a tight-binding lattice. The momentum operator introduces hopping elements v between nearest-neighbor sites. The transparency of the left and right contacts is parameterised by a factor $\tau \in [0, 1]$, introduced in the hopping matrix $v_0 = \tau v$ across the two interfaces, see Appendix A. G_N is calculated by means of the Greens function

technique^{67,68},

$$G_N = 4 \frac{e^2}{h} \text{Tr}[\Gamma_L G^r \Gamma_R G^a] \quad (2)$$

where $G^r = g_0^r + g_0^r \Sigma^r G^r = (G^a)^\dagger$ is the full retarded Green's function. The bare Green's function of the normal region without the presence of the leads is $g_0^r = [\omega - h_0 + i0^+]^{-1}$. The hamiltonian h_0 corresponds to H_0 in Eq. 1 with $\mu_{leads} = \mu_{nw}$. The leads are taken into account through the self-energies $\Sigma_{L(R)}^r = v g_{L(R)}^r v^\dagger$, where $g_{L(R)}^r = [\omega - h_{L(R)} + i0^+]^{-1}$ stands for the left/right lead's propagator, when decoupled from the system. In this case, $h_{L(R)}$ corresponds to H_0 in Eq. (1) with $\mu = \mu_{leads}$. Finally, $\Gamma_{L(R)} = \frac{\Sigma_{L(R)}^r - \Sigma_{L(R)}^a}{2i}$. In practice, G_N is computed recursively with the boundary conditions imposed by the leads.

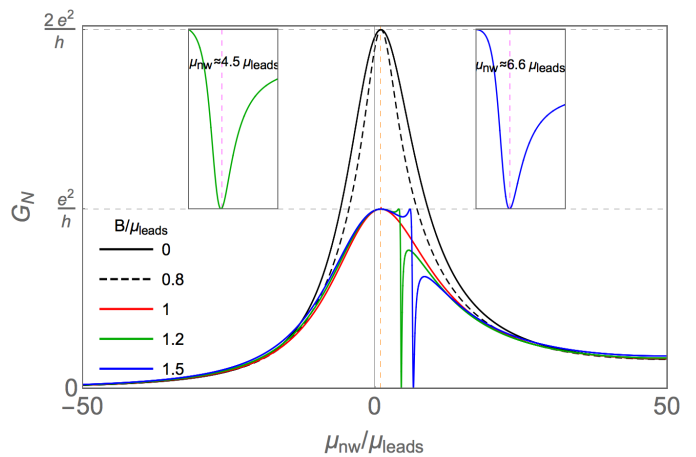


FIG. 2. (Color online) Normal conductance G_N as a function of the Fermi energy μ_{nw} for a short N-NW-N junction, $L_{nw} = 20 \text{ nm}$ (rest of parameters $E_{SO} = 0.05 \text{ meV}$ and $\mu_{leads} = 10 E_{SO}$). Different curves show how $G_N(\mu_{nw})$ evolve with the Zeeman field B . The insets show a blow-up of $G_N(\mu_{nw})$ around the Fano dip for two different B .

To set the stage, we first consider an NW-N junction between a semi infinite nanowire and a good metal, which will allow us to discuss deviations when we consider confinement effects. Fig. 1 shows the expected conductance profile as a function of the NW Fermi energy μ_{nw} , for different values μ_{lead} of the Fermi energy in the metal. At finite magnetic fields, the normal conductance exhibits a gap (with $G_N \approx e^2/h$) of size $\Delta\mu_{nw} = 2B$. As we explained, this gap is a direct consequence of the combined action of Zeeman effect and strong SO coupling and reflects the presence of helical transport, namely spin-polarized counter propagating states⁶⁵. As discussed in Ref. 66, the visibility of this helical gap depends on various factors which, importantly, include the actual value of the SO energy. Indeed, as the ratio μ_{lead}/E_{SO} is made larger, the visibility of the gap in G_N is rapidly degraded (see lower curves in Fig. 1).

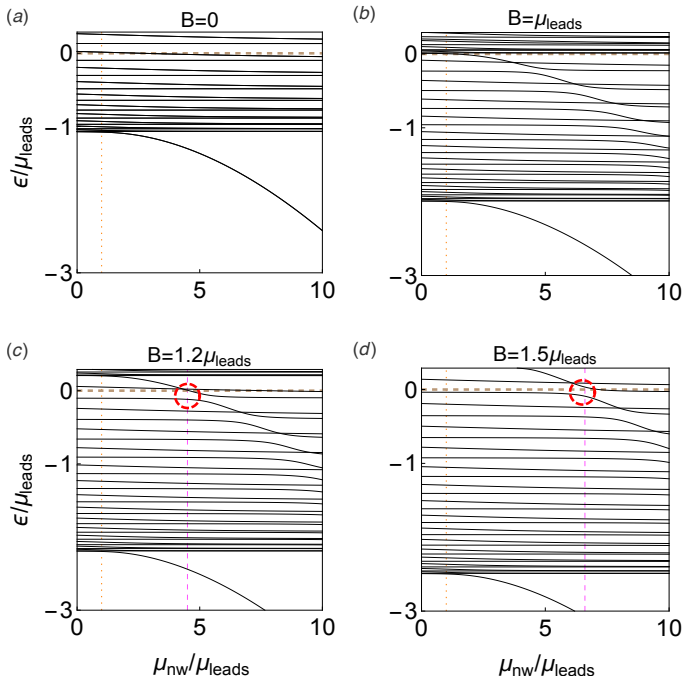


FIG. 3. (Color online) Energy levels as a function of the Fermi energy μ_{nw} for the same system as in Fig. 2. Different panels show how the levels evolve with the Zeeman field B . The red dashed circle shows the value of μ_{nw} for which one of the projections of the Zeeman-split bound state resonates with carriers at the Fermi level (horizontal dashed line), leading to a Fano resonance in conductance.

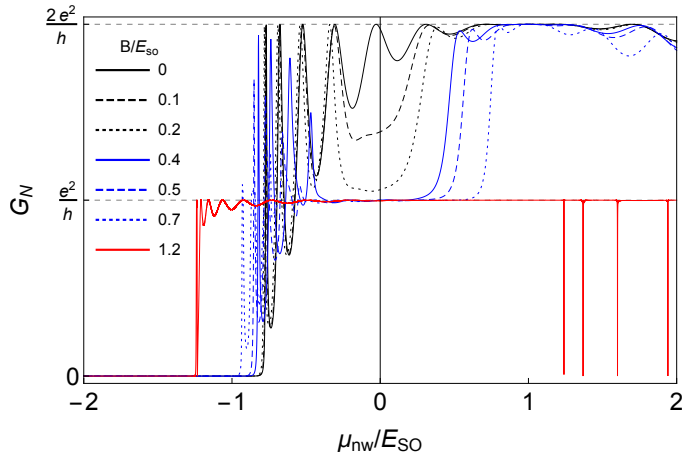


FIG. 4. (Color online) Normal conductance G_N as a function of the Fermi energy μ_{nw} for a long junction with $L_N = 4\mu m$, $E_{SO} = 0.05$ meV and $\mu_{leads} = E_{SO}$. For intermediate magnetic fields, $B \leq E_{SO}$ the conductance develops a clear helical gap inside the Fabry-Perot resonant structure. This gap signals the region where the middle section of the NW becomes helical. When $B \geq \mu_{leads}$, the contacts become helical too and the conductance shows helical Fano dips (red curve).

We now consider the confined N-NW-N junction geometry. Due to the confinement of the central NW section,

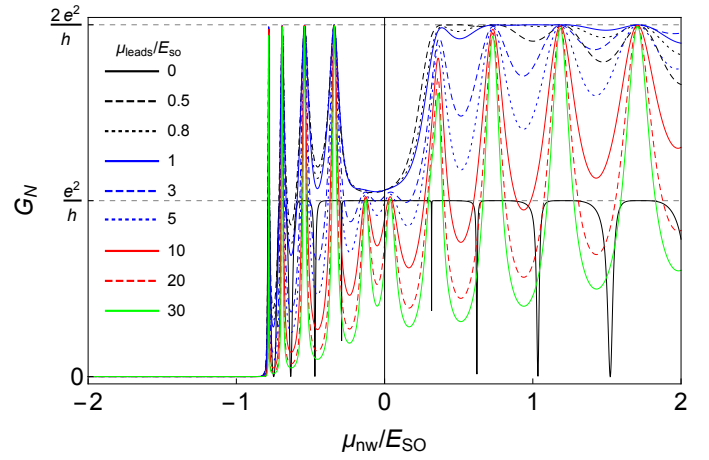


FIG. 5. (Color online) Same as Fig. 4 for fixed magnetic field $B = 0.2E_{SO}$ and increasing μ_{leads} . The helical Fano dips are only seen for $\mu_{leads} < B$ (solid line).

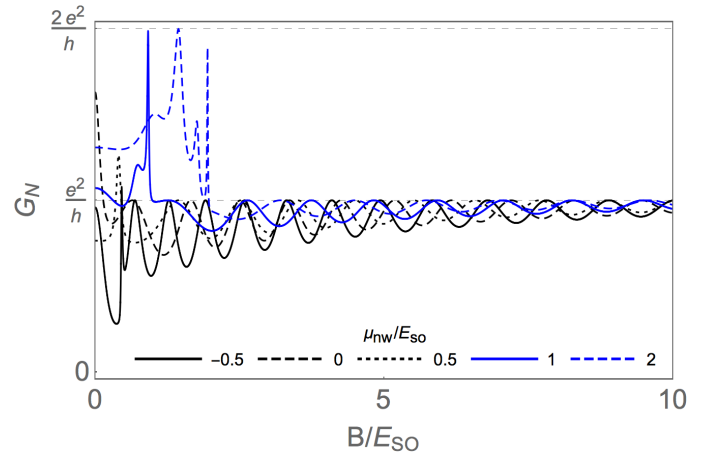


FIG. 6. (Color online) Normal conductance G_N as a function of magnetic field for different values of the Fermi energy μ_{nw} (same parameters as in Fig. 4, except $\mu_{leads} = 10E_{SO}$). The oscillatory behavior when $B > \mu_{nw}$ reflects the transition to the helical regime in the normal side.

Fabry-Perot resonances are expected. Fig. 2 shows the extreme case of a very short central region with only one resonant quasibound state in the junction. As expected, the conductance without external Zeeman field (solid curve) has a Lorentzian shape and reaches its maximum value $G_N = 2e^2/h$ when $\mu_{nw} = \mu_{leads}$ (vertical dashed guideline). Similar results are found for small Zeeman fields $B < \mu_{leads}$ (dashed). When $B = \mu_{leads}$, however, the leads become spin-polarized (or helical, to be precise) and hence the maximum conductance is halved to $G_N = e^2/h$ (red curve).

We consider first the situation with $B > \mu_{leads}$. This regime is characterized by strong Fano dips that appear when μ_{nw} is positive, namely when the junction is gated to create a quantum dot instead of a barrier, see Eq. (1). At these Fano dips destructive interference is maxi-

mum and $G_N = 0$. Moreover, the position of these Fano resonances moves to higher μ_{nw} as B increases (Fig. 2, insets). The Fano dips can be understood by noticing that the system develops a truly bound state at an energy below μ_{leads} as μ_{nw} increases (Fig. 3a). While for $B \ll \mu_{\text{leads}}$ this level lies far below the chemical potential of the leads and cannot significantly affect G_N , in the case $B > \mu_{\text{leads}}$ at hand, the situation is markedly different. At such high fields, one spin sector in the leads is removed away from the chemical potential, and the leads become helical. Similarly, the bound state below μ_{leads} is Zeeman-split, such that the component corresponding to the removed spin sector may then cross the Fermi level at a given μ_{nw} (Fig. 3b-d). This results in one spin projection strongly coupled to the continuum (the sector that is not removed), while the other spin projection remains weakly coupled to this helical continuum through the split bound state (dashed circles), owing to the small spin canting induced by SO. This configuration mimics the physics of a Fano resonance, as we explicitly demonstrate in Appendix B with an effective model. Note that SO is essential to mimic the physics of the Fano effect (two channels with very different coupling to the continuum). Indeed, we have checked that for $\alpha_R = 0$ (namely a fully spin-polarized system without canting) the effect disappears (not shown). The general behavior is related to the so-called Fano-Rashba effect in systems with inhomogeneous Rashba couplings^{69,70} although in our case the bound states originate from the Fermi energy inhomogeneity, which is probably more realistic for NWs with gates. For intermediate lengths, the system can accommodate many of the above resonances but the helical gap is not visible (not shown).

Consider now the $B < \mu_{\text{leads}}$ regime complementary to the preceding discussion. In this situation, there exist two propagating channels in the leads, and conductance may reach $2e^2/h$ at Fabry-Perot maxima, as long as the central NW is likewise non-helical ($B > |\mu_{\text{nw}}|$). Otherwise, for long enough junctions ($L_{\text{nw}} \geq 4\mu\text{m}$ for the realistic NW parameters in our simulation) a helical gap develops in conductance, such that $G_N \lesssim e^2/h$. As central μ_{nw} is tuned into and out of the helical regime, conductance exhibits a reentrant behavior, switching from $\sim 2e^2/h$ to e^2/h and back to $2e^2/h$. This reentrance can be resolved across multiple resonant helical Fabry-Perot oscillations. This is illustrated in Fig. 4 where we plot the conductance for a $4\mu\text{m}$ -long nanowire as a function of the central Fermi energy μ_{nw} . Note the reentrant conductance, and the helical Fabry-Perot resonances with an e^2/h ceiling, signalling helical transport in the junction. The visibility of the conductance reentrance and the helical gap is lost for fields $B > E_{SO}$, see bandstructure inset in Fig. 1. At such fields, the helical gap becomes an extended $G_N \sim e^2/h$ half-plateau (potentially with superimposed Fano resonances if B also exceeds μ_{leads}) that emerges directly from pinch-off $G_N = 0$. Note that the regime with helical Fano dips in the normal conductance is quite relevant towards reaching topological su-

perconductivity: the NW under the contacts can become a non-trivial topological superconductor in the presence of pairing as long as it can be depleted and made helical in the normal phase. Hence our prediction of helical Fano dips superimposed on a half-plateau of $G_N \sim e^2/h$ constitutes a strong signature of helical behavior as precursor of non-trivial superconductivity.

Similar phenomenology is obtained for conductance at fixed magnetic fields and increasing μ_{leads} (Fig. 5). As expected, the Fano dips disappear as soon as $\mu_{\text{leads}} > B$ while the gap coming from helicity in the central section in the NW is much more robust. Increasing μ_{leads} results in well defined Fabry-Perot resonances in the helical gap region. The normal conductance as a function of magnetic field is shown in Fig. 6. Here, a change from irregular behavior to regular e^2/h oscillations as a function of magnetic field signals the helical regime when $B \geq \mu_{\text{nw}}$ ⁶⁶.

Having in mind that there exists no conclusive experimental evidence of the helical regime in nanowires in the literature^{71,72}, the nontrivial resonant effects in finite-length junctions that we have described, both helical Fabry-Perot resonances and helical Fano dips, could be used as an interesting option for detecting such helical transport regime in long junctions. Even more significant, these helical resonant features give rise to a non-trivial subgap spectrum when the leads become superconducting, as we discuss in what follows.

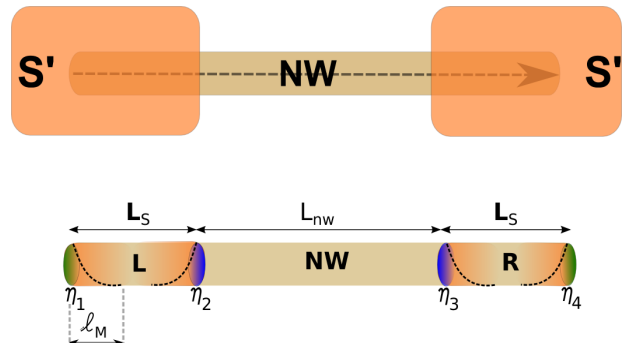


FIG. 7. (Color online) Two s-wave superconductors (S' , with gaps $\Delta_{S'}$) linked by a Rashba nanowire (NW) of length $L = L_S + L_{\text{nw}} + L_S$. Superconductors induce superconducting correlations into the nanowire via proximity effect, giving rise to regions we refer to as superconducting leads (left L and right R) with gaps $\Delta < \Delta_{S'}$ and Fermi energies μ_{leads} , and a central region in the normal state with μ_{nw} . The bold arrow in the first figure denotes the applied Zeeman field along the NW. Due to the finite length L_S , the junction in the topological phase has four Majorana bound states, $\eta_1, \eta_2, \eta_3, \eta_4$, with localization length ℓ_M .

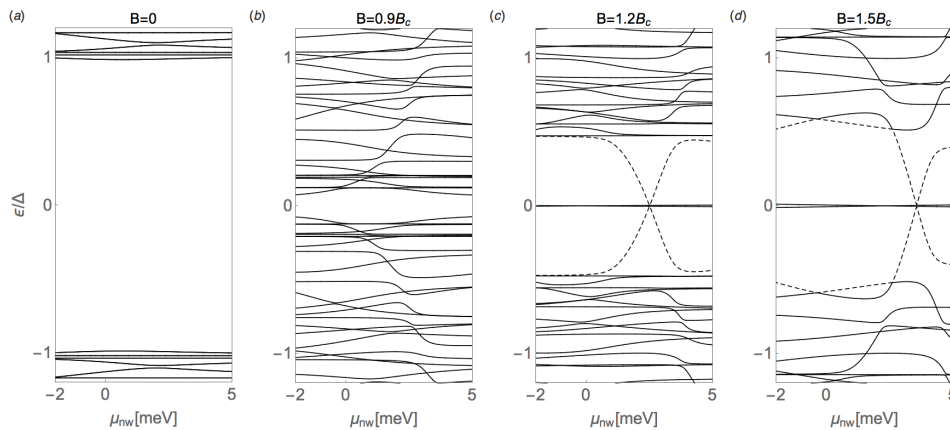


FIG. 8. Andreev levels at $\varphi = 0$ of a short junction, $L_{\text{nw}} = 20$ nm as a function of μ_{nw} . Different panels show the evolution of the spectrum for increasing magnetic fields. Parameters: $E_{SO} = 0.05$ meV, $\mu_{\text{leads}} = 10E_{SO}$, $L_S = 2\mu\text{m}$, $\Delta = 0.25$ meV.

IV. SUBGAP LEVELS IN SNS JUNCTIONS

A. SNS junction model and relevant length scales

To model a SNS junction we assume that the outer parts of the wire are coupled to an s-wave superconductor (with bulk values $\mu_{S'}$ and pairing $\Delta_{S'}$), while the central is not (see Fig. 7). Superconducting correlations are induced by proximity effect into the nanowire. The regions of the nanowire below the superconducting contacts acquire superconducting properties which we refer to as superconducting leads with equal Fermi energy μ_S and pairing potential on the left (L) and right (R) contact given by $\Delta_L = \Delta e^{-i\varphi/2}$ and $\Delta_R = \Delta e^{i\varphi/2}$, where $\Delta < \Delta_{S'}$. The region in the middle of the nanowire without superconducting correlations is the normal region (N) with Fermi energy denoted by μ_{nw} as before. At high enough magnetic fields, the regions of the NW below the superconductors (S regions of the junction) can be driven into a topological superconducting phase when $B > B_c \equiv \sqrt{\mu_S^2 + \Delta^2}$. Owing to the finite length L_S , this results in a SNS junction with four Majorana bound states: two inner Majorana bound states, labeled $\eta_{2,3}$, that form inside the junction, and two outer Majorana bound states, $\eta_{1,4}$, see Fig. 7.

SNS Josephson junctions are classified in two types, depending on the relationship between the length of the normal region L_{nw} (i.e. distance between the superconducting contacts) and the coherence length $\xi = 2\hbar v_F/\pi\Delta$, where v_F is the Fermi velocity. Short junctions are characterized by $L_{\text{nw}} \ll \xi$, whereas $L_{\text{nw}} \gg \xi$ in long junctions. Such classification can be also given in terms of natural energy scales of the problem, the Thouless energy, $E_T = \hbar v_F/L_{\text{nw}}$, and the induced superconducting pair potential Δ , being v_F the Fermi velocity, and L_{nw} the length of the normal region. The above conditions, in terms of these energy scales, are $\Delta \ll E_T$ for short junctions and $\Delta \gg E_T$ for long ones. The significance of this classification is related to the typical

number $\sim \Delta/E_T$ of Andreev subgap states of the junction, in addition to the MBSs at zero energy.

The MBSs wave functions decay from both ends of the topological superconducting leads. The inner and outer MBSs may feel their mutual presence if their wave functions exhibit a non zero spacial overlap. The relevant decay distance characterizing this overlap is the Majorana localization length ℓ_M (appendix C). For finite $L_S < 2\ell_M$ the overlap between MBSs is significant and therefore they are no longer true zero modes.

In what follows, we discuss the subgap spectrum of short SNS junctions in the topological regime $B > B_c$ as well as the subgap spectrum of long SNS junctions as one goes from the *helical* junction regime to the topological one. The helical junction regime is defined by a central region is depleted into the helical regime, while the S regions remain non-topological, namely by $\mu_S > \mu_{\text{nw}}$, and $\mu_{\text{nw}} < B < B_c$.

B. Short junctions

For very short junctions, the ABS spectrum at $B < B_c$ and $\varphi = 0$ does not contain sub-gap states (Figs. 8a and b). This is expected for a short junction with $\xi \gg L_N$. The $B > B_c$ spectrum (Figs. 8c and d), on the other hand, is much more interesting. It contains the expected subgap state near zero energy for all μ_{nw} (coming from the weakly coupled outer Majoranas for $L_S > \ell_M$, the inner MBS at $\varphi = 0$ are strongly hybridized and form standard ABS at energy $\sim \Delta$). Notably, this MBS coexists with a bound state that crosses zero energy for a given $\mu_{\text{nw}} > 0$ (dashed line). This bound state originates from the single resonance that the junction accommodates for increasing $\mu_{\text{nw}} > 0$ (see Fig. 3), which we discussed in connection to Fano resonances. If we interpret this resonant state as an impurity level, our results for $B < B_c$ are consistent with Anderson's theorem which prevents the existence of bound states inside the gap of an s-wave superconductor for non-magnetic impurities⁷³.

The reason is that the zero-energy crossing appears for $B > B_c$, such that the superconductor is effectively p-wave. Therefore, the emergence of these subgap states crossing zero energy should be understood as a direct consequence of nontrivial topology in the junction^{59,60}. The precise condition for the level crossing coincides with the condition for having a Fano dip. As we discussed in section III, this is the condition in the normal regime for having a single resonant state which interferes destructively with a helical contact; the latter condition is here fulfilled because $\mu_{\text{leads}} < B_c < B$. These subgap states and zero-energy crossings should be understood as the p-wave counterparts of so-called Yu-Shiba-Rusinov sub-gap states⁶¹⁻⁶⁴ and their corresponding parity crossings⁷⁴ in s-wave superconductors with magnetic impurities.

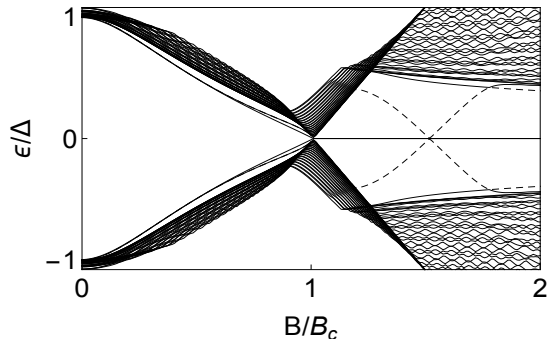


FIG. 9. Andreev levels at $\varphi = 0$ as function of the Zeeman field for $\mu_{\text{nw}} = 3.57$ meV. The rest of parameters are the same as in Fig. 8 except $L_S = 10\mu m$.

Further insight comes from the magnetic field dependence at fixed μ_{nw} (Fig. 9). After the closing of the gap across the topological phase transition at $B = B_c$, the spectrum of the junction exhibits a perfect zero-energy state accompanied by a zero-energy crossing (dashed line) similar to the one discussed in Fig. 8. Note here that, despite the finite length of the central NW, the zero energy state for $B > B_c$ does not oscillate as a function of Zeeman field, unlike what is typical of overlapping MBSs^{36,75-77}. This can be easily understood as this state comes from the *outer* MBSs which at $\varphi = 0$ are effectively decoupled across the junction, since we assume $L_S \gg \ell_M$.

We now analyze in more detail the full phase dependence in the topological phase for different values of μ_{nw} . The low-energy sector is characteristic of a short junction: two almost φ -independent levels near zero energy coming from outer MBSs and two dispersive levels coming from hybridization of inner MBSs across the junction. The anti crossings near $\varphi = \pi$ are only visible for finite L_S/ℓ_M . For $L_S \gg \ell_M$ (Fig. 10a), the zero-energy levels are flat and the anti crossing at $\varphi = \pi$ becomes negligible⁷⁸. In the following, we refer to the dispersive ABS with almost perfect crossings at $\varphi = \pi$ as Majorana ABSs. As μ_{nw} increases, an extra bound state emerges from the continuum as an almost dispersion less subgap

state and interacts very weakly with the Majorana ABSs (Fig. 10b). Importantly, after crossing zero energy (Fig. 10c) and reemerging at finite energy (Fig. 10d), the anti crossing with the Majorana ABS is considerably larger, indicating that the bound state has changed its parity character.

C. Long junctions

The ABS spectrum of long junctions at small magnetic fields $B < B_c$ differs considerably from the one of short junctions. Even for $B = 0$ (Fig. 11a), the spectrum is very sensitive to the sharp increase of conductance at small negative μ_{nw} , when the junction goes rapidly from pinch-off to fully transmitting (solid black line in Fig. 4). This is reflected in a feature that resembles the closing and reopening of a gap (but, of course, is related to the central region becoming metallic, rather than with a gap closing). The emergence of Fabry-Perot resonances in the normal phase is translated into the appearance of level pairs at finite energies, or loops, that oscillate with system parameters in the superconducting phase. A distinct change in the loop structure takes place as B is increased within a window $|\mu_{\text{nw}}| < B$. This, recall, corresponds to the helical regime of the normal region, characterised in normal transport by a helical gap and helical Fabry-Perot oscillations. The loops inside said window reconnect, and give rise to new loops around zero-energy, separated by parity crossings (Fig. 11b). Each of these crossings corresponds to a helical Fabry-Perot resonance in the normal regime. For larger Zeeman energies, supporting many helical Fabry-Perot resonances within the helical gap, correspondingly many consecutive zero-energy loops become visible in the superconducting regime. As soon as the normal side ceases to be helical ($|\mu_{\text{nw}}| > B$), the spectrum does no longer show loops around zero energy. Since depleting the normal section of the NW junction should be much easier than gating the proximized region, we expect that said near-zero loops and parity crossings should be ubiquitous for finite size junctions near depletion⁷⁹ and constitute yet another alternative scheme to detect the helical regime.

Each loop in the helical regime (see e.g. Fig. 11b) is similar to the ones expected for magnetic impurities⁶¹⁻⁶⁴, or quantum dots in the Coulomb blockade regime^{30,47} coupled to superconductors (we emphasize here that our junction is noninteracting). This result again suggests an interesting analogy with the physics of Yu-Shiba-Rusinov states in superconductors with magnetic impurities. Here, the combined action of Zeeman-induced spin-polarization *and depletion* is crucial.

Consecutive loops around zero energy, resemble the oscillatory behavior expected from overlapping MBSs in finite length NWs. However, since the helical gap condition $|\mu_{\text{nw}}| < B$ does not involve μ_S , which may be large, the zero-energy loops may exist while the proximized S regions are still in the topologically trivial regime $B < B_c$

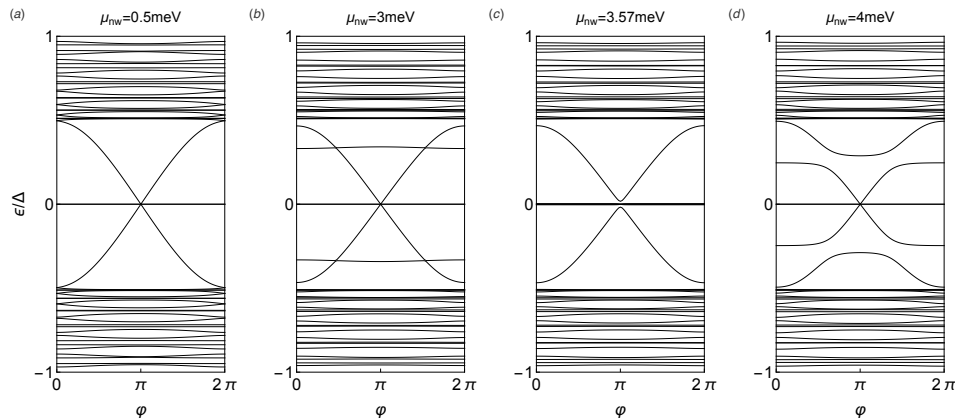


FIG. 10. Andreev levels at the junction $\epsilon(\varphi)$ in the short-junction regime, $L_{\text{nw}} = 20 \text{ nm}$ in at $B = 1.5B_c$. Parameters: $\alpha_R = 20 \text{ meV nm}$ for InSb nano wires, $\mu_S = 0.5 \text{ meV}$, $L_S = 10 \mu\text{m}$, and $\Delta = 0.25 \text{ meV}$. Different panels show the Andreev levels around $\mu_{\text{nw}} = 3.57 \text{ meV}$ near the zero-energy crossing in Fig. 8d.

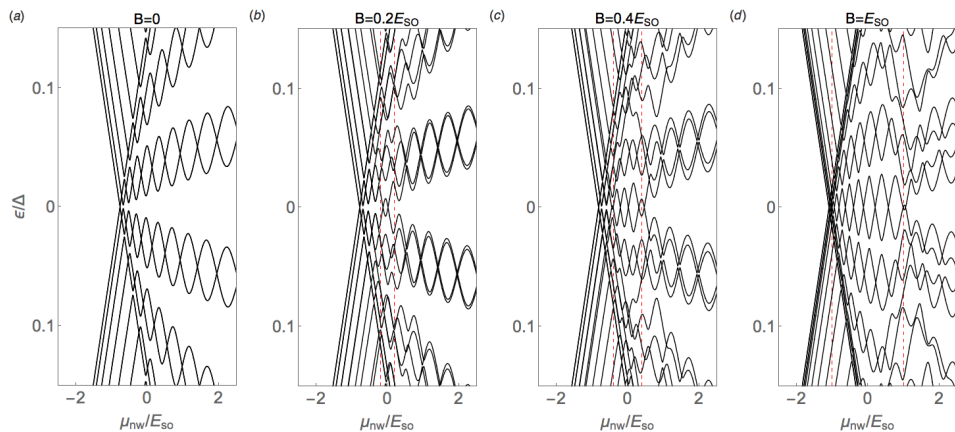


FIG. 11. Andreev levels at $\varphi = 0$ as function of μ_{nw} for a long junction, $L_{\text{nw}} = 4 \mu\text{m}$ and various magnetic fields. Parameters: $E_{SO} = 0.05 \text{ meV}$, $\mu_S = 10E_{SO}$, $L_S = 2 \mu\text{m}$, $\Delta = 0.25 \text{ meV}$. At finite B, the ABS spectrum shows a loop structure around zero energy in the region where the normal side becomes helical (marked by dashed lines). Note that the junction is very far from becoming topological ($B_c \approx 11.2E_{SO}$).

(Fig. 11 c and d). Remarkably, there exists a profound connection between zero-loops and MBSs. We find that the former actually evolve continuously into outer MBSs as B is increased beyond B_c . To illustrate this key idea, we compare in Fig. 12, a situation without near-zero energy loops at low B fields ($\mu_{\text{nw}} = \mu_S$, panel a) with another with loops at very low B coming from a helical normal region ($\mu_{\text{nw}} = 0$, panel a). While the MBSs in the first configuration emerge from a situation without zero energy states/crossings at low fields, the ones corresponding to the second configuration are clearly evolving from the low B-field loops around zero energy. We emphasize here that both configurations correspond to the same physical nanowire junction with the sole difference of a depletion in the *normal part* of the junction in the second case. Fig. 12 nicely illustrates two of our main results: 1) long loops with parity crossings in the ABS spectrum can be used to identify the helical regime in a Rashba NW and 2) such helical loops, coming from de-

pletion in the *normal* side of the junction, continuously evolve into MBS for large enough magnetic fields.

To obtain more precise information about the nature of this interesting connection between $B < B_c$ near-zero loops and MBS states, we study their evolution for increasing SO coupling (Fig. 13). For $\alpha_R = 0$ (Fig. 13a), Zeeman-induced depairing closes the superconducting gap and the spectrum becomes a dense quasi-continuum (the full junction is in the normal regime), as expected. Any $\alpha_R \neq 0$ removes all finite energy crossings while preserving the parity-protected crossings at zero energy. As a result, the spectrum is still gapped after the first parity crossing (the Zeeman field is no longer fully depairing) and *many parity crossings* are possible. This important observation is illustrated in Fig. 13(b,c) (see also Fig. 12b). For finite α_R , the low-energy spectrum remains gapped after the first crossing and also after subsequent crossings. Another interesting conclusion that we can draw from our results is that a clear distinction

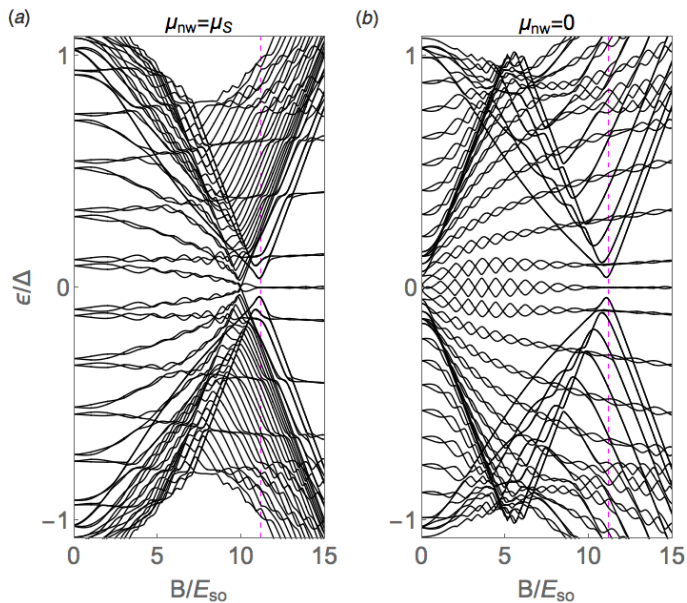


FIG. 12. Andreev levels at $\varphi = 0$ as function of B . Same parameters as in Fig. 11. The critical field B_c is marked by vertical dashed line.

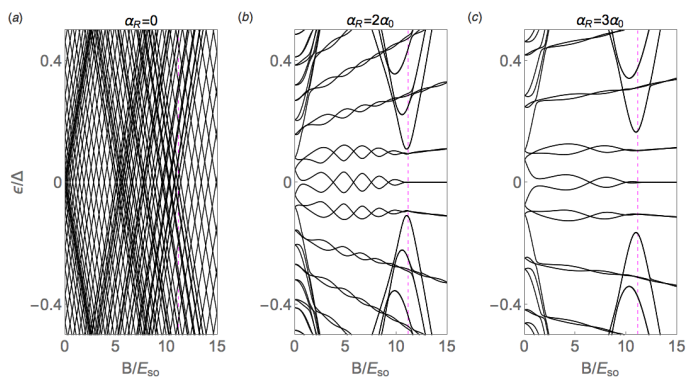


FIG. 13. Same as Fig. 12 for $\mu_{\text{nw}} = 0$ and increasing values of the SO coupling α_R . The critical field B_c is marked by vertical dashed line.

between the near-zero states in the $B < B_c$ and $B > B_c$ regions can no longer be made. The only difference is quantitative, in that the amplitude of MBS oscillations in the topological regime become smaller for increasing α_R , unlike for $B < B_c$. (The SO length becomes much shorter and, hence $L_S \gg \ell_M$). However, other spectral properties, such as the mini gap separating the near-zero modes from the first excited states, is roughly the same in both the trivial $B < B_c$ and non-trivial $B > B_c$ phases.

To finish, we consider the phase dependence of the subgap spectrum. While topological SNS junctions with $L_S \rightarrow \infty$ are 4π -periodic as a function of phase difference ϕ due to the characteristic parity-protected crossing at $\phi = \pi$ (see e.g. Fig. 8a), in finite L_S junctions (Fig. 14a), said crossing is avoided, and splits by a small energy due to the hybridization of MBSs at the junction

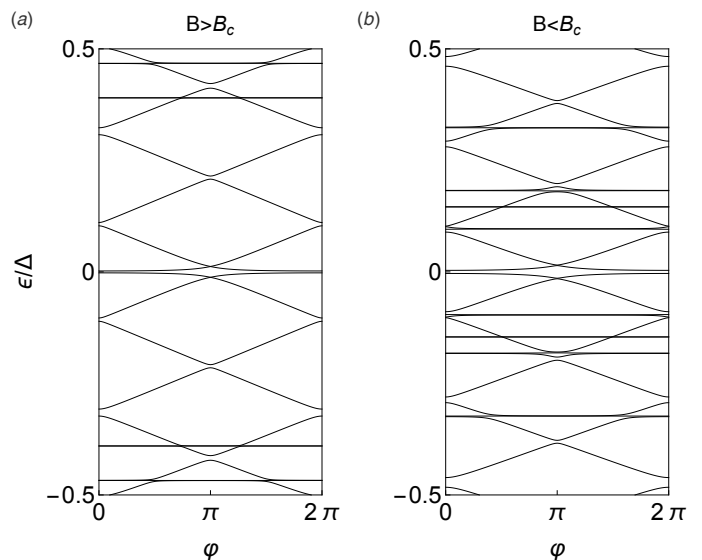


FIG. 14. Andreev levels as function of phase φ for two values of the Zeeman field a) $B = 10E_{SO}$ and b) $B = 13E_{SO}$. Rest of parameters same as in Fig. 12b.

(inner) and MBSs at the far ends of each S region (outer), which leads to a more conventional 2π -periodicity⁸⁰. Interestingly, the subgap spectrum at $B < B_c$ (Fig. 14b) shows essentially the same phase-dependence which further confirms the deep connection between the $B < B_c$ and $B > B_c$ parity crossings. Note that the resulting Josephson current, which only depends on the Andreev spectrum, would be effectively the same (not shown).

V. CONCLUSIONS

We have studied the normal transport and the subgap spectrum of SNS junctions based on semiconducting nanowires with strong Rashba spin-orbit coupling. In particular, we have focused on the role of confinement effects in ballistic finite-length junctions and analyzed the distinct properties of the ABS for short and long junctions as different sections of the underlying NW (N or S or both) become helical. For $B > B_c$, confined levels in the normal section give rise to bound subgap states, as expected from the effective p-wave nature of the topological superconductor. In normal transport, such bound states give rise to helical Fano dips. Perhaps more strikingly, we have found that a long junction with a helical normal section, but still in the topologically trivial regime with $\mu_{\text{nw}} < B < B_c$, supports a low-energy subgap spectrum consisting of multiple-loop structures and parity crossings. Such states are derived from helical Fabry-Perot resonances in the normal regime. We have argued that such multiple loop structure in the ABS spectrum could be used to unambiguously identify the helical regime in NWs. Interestingly, these multiple loops smoothly evolve towards Majorana bound states as the Zeeman field ex-

ceeds the critical value. This suggests an interesting connection between subgap parity crossings in helical junctions with $B < B_c$ and Majorana bound states in topological ones with $B > B_c$. A recent study of fully open helical-N/trivial-S contacts⁸¹ further confirms the profound connection between subgap states in the helical regime and Majorana physics.

VI. ACKNOWLEDGEMENTS

We acknowledge the support of the European Research Council and the Spanish Ministry of Economy and Inno-

vation through the JAE-Predoc Program (J. C.), Grants No. FIS2011-23713 (P. S.-J), FIS2012-33521 (R. A.), FIS2013-47328 (E. P.) and the Ramón y Cajal Program (E. P.).

-
- ¹ E. Majorana, *Nuovo Cimento*, 171 (1937).
² F. T. Avignone, S. R. Elliott, and J. Engel, *Rev. Mod. Phys.* **80**, 481 (2008).
³ F. Wilczek, *Nat Phys* **5**, 614618 (2009).
⁴ S. R. Elliot and M. Franz, arXiv:1403.4976 (2014).
⁵ For reviews, see J. Alicea, *Rep. Prog. Phys.* **75**, 076501, (2012); C. Beenakker, *Annu. Rev. Cond. Mat. Phys.* **4**, 113, (2013); T. Stanescu and S. Tewari, *J. Phys. Condens. Matter* **25**, 233201, (2013).
⁶ M. Z. Hasan and C. L. Kane, *Rev. Mod. Phys.* **82**, 3045 (2010).
⁷ X.-L. Qi and S.-C. Zhang, *Rev. Mod. Phys.* **83**, 1057 (2011).
⁸ In fact they obey non-Abelian exchange statistics which might have potential applications in fault-tolerant quantum computation⁸².
⁹ Recently, it has been argued that Bogoliubov quasiparticles in conventional superconductors are true Majorana fermions, see C. Chamon, R. Jackiw, Y. Nishida, S.-Y. Pi and L. Santos, *Phys. Rev. B* **81**, 224515, (2010). Their Majorana fermion nature can be revealed by annihilation processes, see C. Beenakker, *Phys. Rev. Lett.* **112**, 070604 (2014).
¹⁰ N. B. Kopnin and M. M. Salomaa, *Phys. Rev. B* **44**, 9667 (1991).
¹¹ G. E. Volovik, *JETP Lett.* **70**, 609 (1999).
¹² T. Senthil and M. P. A. Fisher, *Phys. Rev. B* **61**, 9690 (2000).
¹³ N. Read and D. Green, *Phys. Rev. B* **61**, 10267 (2000).
¹⁴ A. Y. Kitaev, *Phys. Usp.* **44**, 131 (2001).
¹⁵ S. Das Sarma, C. Nayak, and S. Tewari, *Phys. Rev. B* **73**, 220502 (2006).
¹⁶ L. Fu and C. L. Kane, *Phys. Rev. Lett.* **100**, 096407 (2008).
¹⁷ M. Sato, Y. Takahashi, and S. Fujimoto, *Phys. Rev. Lett.* **103**, 020401 (2009).
¹⁸ J. D. Sau, R. M. Lutchyn, S. Tewari, and S. Das Sarma, *Phys. Rev. Lett.* **104**, 040502 (2010).
¹⁹ J. Alicea, *Phys. Rev. B* **81**, 125318 (2010).
²⁰ R. M. Lutchyn, J. D. Sau, and S. Das Sarma, *Phys. Rev. Lett.* **105**, 077001 (2010).
²¹ Y. Oreg, G. Refael, and F. von Oppen, *Phys. Rev. Lett.* **105**, 177002 (2010).
²² K. Sengupta, I. Zutik, H.-J. Kwon, V. M. Yakovenko, and S. Das Sarma, *Phys. Rev. B* **63**, 144531 (2001).
²³ C. J. Bolech and E. Demler, *Phys. Rev. Lett.* **98**, 237002 (2007).
²⁴ K. T. Law, P. A. Lee, and T. K. Ng, *Phys. Rev. Lett.* **103**, 237001 (2009).
²⁵ V. Mourik, K. Zuo, S. Frolov, S. Plissard, E. Bakkers, and L. Kouwenhoven, *Science* **336(6084)**, 1003 (2012).
²⁶ M. T. Deng, C. L. Yu, G. Y. Huang, M. Larsson, P. Caroff, and H. Q. Xu, *Nano Lett.* **12**, 6414 (2012).
²⁷ A. Das, Y. Ronen, Y. Most, Y. Oreg, M. Heiblum, and H. Shtrikman, *Nat Phys* **8**, 887 (2012).
²⁸ A. D. K. Finck, D. J. Van Harlingen, P. K. Mohseni, K. Jung, and X. Li, *Phys. Rev. Lett.* **110**, 126406 (2013).
²⁹ H. O. H. Churchill, V. Fatemi, K. Grove-Rasmussen, M. T. Deng, P. Caroff, H. Q. Xu, and C. M. Marcus, *Phys. Rev. B* **87**, 241401 (2013).
³⁰ E. J. H. Lee, X. Jiang, M. Houzet, R. Aguado, C. M. Lieber, and S. D. Franceschi, *Nat. Nanotech.* **9**, 79 (2014).
³¹ E. J. H. Lee, X. Jiang, R. Aguado, G. Katsaros, C. M. Lieber, and S. De Franceschi, *Phys. Rev. Lett.* **109**, 186802 (2012).
³² F. Pientka, G. Kells, A. Romito, P. W. Brouwer, and F. von Oppen, *Phys. Rev. Lett.* **109**, 227006 (2012).
³³ D. Bagrets and A. Altland, *Phys. Rev. Lett.* **109**, 227005 (2012).
³⁴ J. Liu, A. C. Potter, K. T. Law, and P. A. Lee, *Phys. Rev. Lett.* **109**, 267002 (2012).
³⁵ J. D. Sau and S. Das Sarma, *Phys. Rev. B* **88**, 064506 (2013).
³⁶ E. Prada, P. San-Jose, and R. Aguado, *Phys. Rev. B* **86**, 180503(R) (2012).
³⁷ G. Kells, D. Meidan, and P. W. Brouwer, *Phys. Rev. B* **86**, 100503 (2012).
³⁸ R. Žitko, J. S. Lim, R. López, and R. Aguado, arXiv:1405.6084 (2014).
³⁹ Quite recently, further evidence of zero-bias anomalies related to Majoranas have been reported in a different setup consisting of a ferromagnetic atomic chain on top of a superconducting substrate. S. Nadj-Perge, *et al*, *Science*, 10.1126/science.1259327 (2014).
⁴⁰ P. San-Jose, J. Cayao, E. Prada, and R. Aguado, *New Journal of Physics* **15**, 075019 (2013).
⁴¹ P. San-Jose, E. Prada, and R. Aguado, *Phys. Rev. Lett.* **112**, 137001 (2014).
⁴² M. T. Deng, C. L. Yu, G. Y. Huang, M. Larsson, P. Caroff, and H. Q. Xu, *Nano Lett.* **12**, 6414 (2012).

- ⁴³ Y.-J. Doh, J. A. van Dam, A. L. Roest, E. P. A. M. Bakkers, L. P. Kouwenhoven, and S. De Franceschi, *Science* **309**, 272 (2005).
- ⁴⁴ T. Nishio, T. Kozakai, S. Amaha, M. Larsson, H. A. Nilsson, H. Q. Xu, G. Zhang, K. Tateno, H. Takayanagi, and K. Ishibashi, *Nanotechnology* **22**, 445701 (2011).
- ⁴⁵ H. A. Nilsson, P. Samuelsson, P. Caroff, and H. Q. Xu, *Nano Lett.* **12**, 228 (2012).
- ⁴⁶ H. Y. Günel, I. E. Batov, H. Hardtdegen, K. Sladek, A. Winden, K. Weis, G. Panaitov, D. Grützmacher, and T. Schäpers, *J. Appl. Phys.* **112**, (2012).
- ⁴⁷ W. Chang, V. E. Manucharyan, T. S. Jespersen, J. Nygård, and C. M. Marcus, *Phys. Rev. Lett.* **110**, 217005 (2013).
- ⁴⁸ J.-D. Pillet, C. H. L. Quay, P. Morfin, C. Bena, A. L. Yeyati, and P. Joyez, *Nature Nanotechnology*. **6**, 965 (2010).
- ⁴⁹ R. S. Deacon, Y. Tanaka, A. Oiwa, R. Sakano, K. Yoshida, K. Shibata, K. Hirakawa, and S. Tarucha, *Phys. Rev. Lett.* **104**, 076805 (2010).
- ⁵⁰ J.-D. Pillet, P. Joyez, R. Žitko, and M. F. Goffman, *Phys. Rev. B* **88**, 045101 (2013).
- ⁵¹ J. Schindele, A. Baumgartner, R. Maurand, M. Weiss, and C. Schönenberger, *Phys. Rev. B* **89**, 045422 (2014).
- ⁵² L. Bretheau, i. m. c. O. Girit, C. Urbina, D. Esteve, and H. Pothier, *Phys. Rev. X* **3**, 041034 (2013).
- ⁵³ A. Kumar, M. Gaim, D. Steininger, A. Levy Yeyati, A. Martin-Rodero, A. K. Huettel, and C. Strunk, (2013), preprint arXiv:1308.1020v3.
- ⁵⁴ M. F. Goffman, R. Cron, A. Levy Yeyati, P. Joyez, M. H. Devoret, D. Esteve, and C. Urbina, *Phys. Rev. Lett.* **85**, 170 (2000).
- ⁵⁵ D. Chevallier, P. Simon, and C. Bena, *Phys. Rev. B* **85**, 235307 (2012).
- ⁵⁶ D. Chevallier, D. Siclet, P. Simon, and C. Bena, *Phys. Rev. B* **88**, 165401 (2013).
- ⁵⁷ Coulomb blockade effects will be discussed elsewhere.
- ⁵⁸ A. V. Kretinin, R. Popovitz-Biro, D. Mahalu, and H. Shtrikman, *NanoLett.* **10**, 3439 (2010).
- ⁵⁹ J. D. Sau and E. Demler, *Phys. Rev. B* **88**, 205402 (2013).
- ⁶⁰ H. Hu, L. Jiang, H. Pu, Y. Chen, and X. Liu, *Phys. Rev. Lett.* **110**, 020401 (2013).
- ⁶¹ L. Yu, *Acta Phys. Sin.* **21**, 75 (1965).
- ⁶² H. Shiba, *Prog.Theor. Phys.* **40**, 435 (1968).
- ⁶³ A. I. Rusinov, *Sov. Phys. JET* **56**, 2047 (1969).
- ⁶⁴ H. Shiba and T. Soda, *Prog.Theor. Phys.* **41**, 25 (1969).
- ⁶⁵ P. Štředa and P. Šeba, *Phys. Rev. Lett.* **90**, 256601 (2003).
- ⁶⁶ D. Rainis and D. Loss, arXiv:1407.8239 (2014).
- ⁶⁷ C. Caroli, R. Combescot, D. Lederer, P. Nozieres, and D. Saint-James, *J. Phys. C: Solid State Phys.* **4**, 2598 (1971).
- ⁶⁸ H. Haug and A. Jauho, *Quantum kinetics in transport and optics of semiconductors*, Vol. 123 (Springer, 2007).
- ⁶⁹ D. Sánchez and L. m. c. Serra, *Phys. Rev. B* **74**, 153313 (2006).
- ⁷⁰ D. Sanchez, L. Serra, and M. Choi, *Phys. Rev. B* **77**, 035315 (2008).
- ⁷¹ C. H. L. Quay, T. L. Hughes, J. A. Sulpizio, L. N. Pfeiffer, K. W. Baldwin, K. W. West, D. Goldhaber-Gordon, and R. de Piccioto, *Nature Physics* **6**, 336 (2010).
- ⁷² I. van Weperen, S. R. Plissard, E. P. A. M. Bakkers, S. M. Frolov, and L. P. Kouwenhoven, *Nanoletters* **13**, 387 (2013).
- ⁷³ P. W. Anderson, *J. Phys. Chem. Solids* **11**, 26 (1959).
- ⁷⁴ A. Sakurai, *Prog.Theor. Phys.* **44**, 1472 (1970).
- ⁷⁵ J. S. Lim, L. Serra, R. López, and R. Aguado, *Phys. Rev. B* **86**, 121103 (2012).
- ⁷⁶ D. Rainis, L. Trifunovic, J. Klinovaja, and D. Loss, *Phys. Rev. B* **87**, 024515 (2013).
- ⁷⁷ S. Das Sarma, J. D. Sau, and T. D. Stanescu, *Phys. Rev. B* **86**, 220506 (2012).
- ⁷⁸ In $L_S \rightarrow \infty$ limit, the outer Majoranas are no longer involved in transport while the levels at $\varphi = \pi$ exactly cross (not shown) giving rise to anomalous 4π -periodic spectrum and Josephson currents if fermionic parity is conserved.
- ⁷⁹ Intermediate L_{nw} junctions also show the same behavior, not shown.
- ⁸⁰ P. San-Jose, E. Prada, and R. Aguado, *Phys. Rev. Lett.* **108**, 257001 (2012).
- ⁸¹ P. San-Jose, J. Cayao, E. Prada, and R. Aguado, (2014), arXiv:1409.7306.
- ⁸² C. Nayak, S. H. Simon, A. Stern, M. Freedman, and S. Das Sarma, *Rev. Mod. Phys.* **80**, 1083 (2008).

Appendix A: The SNS junction model

In this appendix we describe the model we use for SNS junctions.

1. Tight-binding discretisation

For computation purposes, we consider a discretisation of the continuum model Eq. (1) for the Rashba nanowire into a tight-binding lattice with a small lattice spacing a . Thus H_0 reads,

$$H_0 = \sum_i c_i^\dagger h c_i + \sum_{\langle ij \rangle} c_i^\dagger v c_j + \text{h.c.} \quad (\text{A1})$$

where the symbol $\langle ij \rangle$ means that v couples nearest-neighbor i, j sites. This discretisation transforms Eq. (1), in terms containing on-site energy h and into nearest-neighbor hopping matrices v which arise from the momentum operator p ,

$$\begin{aligned} h_{ii} &\equiv h = \begin{bmatrix} 2t - \mu & B \\ B & 2t - \mu \end{bmatrix}, \\ h_{i+1,i} &\equiv v = \begin{bmatrix} -t & \frac{\hbar}{2a} \alpha_{so} \\ -\frac{\hbar}{2a} \alpha_{so} & -t \end{bmatrix} = h_{i,i+1}^\dagger, \end{aligned} \quad (\text{A2})$$

are matrices in spin space and $t = \hbar^2/2m^*a^2$.

2. The SNS junction model

The Hamiltonian of the full system considering the left and right superconducting leads and the normal region is given by

$$h_{SNS} = \begin{bmatrix} h_{S_L} & h_{S_L N} & 0 \\ h_{S_L N}^\dagger & h_N & h_{N S_R} \\ 0 & h_{N S_R}^\dagger & h_{S_R} \end{bmatrix}, \quad (\text{A3})$$

where h_{S_i} is the Hamiltonian of the superconducting lead $i = L/R$ that we consider to be the same, $h_{S_i N}$ the Hamiltonian that couples the superconducting lead i to the normal region, while $h_{N S_i}$ the Hamiltonian that couples the normal region to the lead i . These coupling matrices are non-zero for adjacent sites that lie at the interfaces of the superconducting leads and of the normal region, only. This coupling is parametrised by a hopping matrix $v_0 = \tau v$ between the sites that define the interfaces of the SNS junction, where $\tau \in [0, 1]$. A tunnel junction can be modelled by considering $\tau \ll 1$, while a full transparent junction with $\tau = 1$. All the elements in the diagonal of matrix Eq. (A3) have the structure of H_0 given by Eq. (1) taking into account that the superconducting lead regions have a Fermi energy μ_S (or μ_{leads} for the normal transport study), while this is μ_{nw} for the normal region. It is important to point out here that the

matrix of Eq. (A3) is of finite size since we are dealing with a fine size system.

Effects of superconductivity are induced by the pairing potential $\Delta(x) = \Delta e^{i\phi}$, thus leading to the Nambu description where the new Hamiltonian reads,

$$H = \begin{bmatrix} h_{SNS} & \Delta(x) \\ \Delta^\dagger(x) & -h_{SNS}^* \end{bmatrix}. \quad (\text{A4})$$

The superconducting pairing potential in the previous Hamiltonian equation, that corresponds to the full system, must have the same structure as the SNS Hamiltonian, h_{SNS} , thus

$$\begin{aligned} \Delta(x) &= \begin{bmatrix} \Delta_{S_L} & 0 & 0 \\ 0 & \Delta_N & 0 \\ 0 & 0 & \Delta_{S_R} \end{bmatrix} \\ &= \begin{bmatrix} \Delta_{0,S} e^{i\phi_L} & 0 & 0 \\ 0 & 0 & 0 \\ 0 & 0 & \Delta_{0,S} e^{i\phi_R} \end{bmatrix}, \end{aligned} \quad (\text{A5})$$

where $\Delta_N = 0$ since in the normal region the superconducting correlations are absent.

Superconductivity is induced by an s-wave pairing potential $\Delta(x)$ that couples particles of different spin and momenta. So that, $\Delta_{0,S}$ is given by

$$\Delta_{0,S} = i\sigma_y \Delta_S = i\sigma_y \Delta. \quad (\text{A6})$$

Appendix B: Model for the conductance

In this part we make use of an effective model to describe the physics of Fano resonances. An effective spinless model based on Green's functions is constructed where two semi-infinite tight-binding chains (leads) are coupled through V to a central region ε_d , formed by one site, that is additionally weakly coupled through $\tau \ll V$ to a resonant level $\varepsilon_0 = \varepsilon_d - \varepsilon_r$, being ε_r a fixed parameter that represents the separation between the quantum dot level and the resonant level (in principle this parameter mimics the role of the Zeeman splitting in our numerics). Consider that a is the lattice constant and t the hopping between sites in the leads. The normal transmission, T_N , through a central system formed by one site can be calculated by using the Caroli's formula,

$$T_N(\omega) = 4 \text{Tr}[\Gamma_L G^r \Gamma_R G^a], \quad (\text{B1})$$

where $G^{r(a)}$ is the retarded (advanced) full system Green's function, and

$$\Gamma_{L(R)}(\omega) = \frac{\Sigma_{L(R)}^r(\omega) - \Sigma_{L(R)}^a(\omega)}{2i}, \quad (\text{B2})$$

takes into account the influence of the leads on the central system through the left(right) L(R) self-energies $\Sigma_{L/R}$. The full system Green's function can be calculated by

using the Dyson's relation,

$$\begin{aligned} G^r(\omega) &= g_0^r(\omega) + g_0^r(\omega) \Sigma^r(\omega) G^r(\omega) = (G^a(\omega))^\dagger \\ \text{or } G^r(\omega) &= [[g_0^r(\omega)]^{-1} - \Sigma^r(\omega)]^{-1}, \end{aligned} \quad (\text{B3})$$

where g_0^r is the retarded Green's function of the isolated central region (this central region can for instance be a quantum dot) without the influence of the leads and without the influence of the resonant level. It reads

$$g_0^r(\omega) = \frac{1}{\omega - \varepsilon_d + i\eta} \quad (\text{B4})$$

where ε_d is the onsite energy of the central region. The self-energy Σ^r ,

$$\Sigma^r(\omega) = \Sigma_L^r(\omega) + \Sigma_R^r(\omega) + \Sigma_{res}^r(\omega) \quad (\text{B5})$$

contain the effect of the left $\Sigma_L(\omega)$ and right $\Sigma_R(\omega)$ leads as well as the influence of the resonant level $\Sigma_{res}(\omega)$, respectively. Such self-energies are defined as follows,

$$\Sigma_{L(R)}^r(\omega) = t^\dagger g_{L(R)}^r(\omega) t \quad (\text{B6})$$

where $g_{L(R)}^r$ is the retarded semi-infinite left (right) lead Green's functions. In principle such lead's Green's functions can be computed considering a recursive approach,

$$g_{L(R)}(\omega) = \frac{1}{\omega - h - t^\dagger g_{L(R)}(\omega) t}, \quad (\text{B7})$$

$h = 2t - \mu$ is the onsite energy in the leads. From previous equation one has,

$$|t|^2 g_{L(R)} - (\omega - h) g_{L(R)} + 1 = 0 \quad (\text{B8})$$

therefore,

$$g_{L(R)}(\omega) = \frac{1}{|t|} \left[\frac{\omega - h}{2|t|} \pm \sqrt{\left(\frac{\omega - h}{2|t|}\right)^2 - 1} \right]. \quad (\text{B9})$$

Adding a convergence factor to frequency, $\omega \rightarrow \omega \pm i\eta$, one finds the retarded or advanced Green's function. We have the following properties of $g_{L(R)}$,

$$g_{L(R)}(\omega) = \begin{cases} \frac{1}{|t|} \left[\frac{\omega - h}{2|t|} - \text{sgn}(\omega - h) \sqrt{\left(\frac{\omega - h}{2|t|}\right)^2 - 1} \right], & |(\omega - h)/2|t| > 1 \\ \frac{1}{|t|} \left[\frac{\omega - h}{2|t|} \pm i \sqrt{1 - \left(\frac{\omega - h}{2|t|}\right)^2} \right], & |(\omega - h)/2|t| < 1 \end{cases} \quad (\text{B10})$$

where for the first case the density of states $\rho_0 = -\frac{1}{\pi} \text{Im} g_{L(R)}$ is zero, while in the second case it exhibits a non zero value. These results allow us to obtain $\Sigma_L^r(\omega)$. The impurity self-energy Σ_{res}^r reads,

$$\Sigma_{res}^r(\omega) = \frac{|\tau|^2}{\omega - \varepsilon_0 + i\eta}, \quad (\text{B11})$$

where τ is the coupling of the resonant level to the system. With these expressions for the different self-energies, we may compute G^r ,

$$G^r(\omega) = \{ [g_0^r(\omega)]^{-1} - \Sigma_L^r(\omega) - \Sigma_R^r(\omega) - \Sigma_{res}^r(\omega) \}^{-1}. \quad (\text{B12})$$

The normal conductance G_N is calculated from the transmission as,

$$G_N = \frac{e^2}{h} \int T_N(\omega) \left(-\frac{df}{d\omega} \right) d\omega \quad (\text{B13})$$

where by construction we have already in a spinless channel. Since we are interested in low temperature physics,

$f(\omega) \approx \Theta(\omega_F - \omega)$, and $df/d\omega \approx -\delta(\omega_F - \omega)$. Therefore,

$$\begin{aligned} G_N &= \frac{e^2}{h} \int T_N(\omega) \delta(\omega_F - \omega) d\omega \\ G_N &= \frac{e^2}{h} T_N(\omega_F), \end{aligned} \quad (\text{B14})$$

where ω_F is the Fermi energy which is the zero of energy in our calculations.

The aim of this part was to construct an effective model that contains the whole physics of our numerics where a resonance in the trivial phase and a dip in the helical phase the transmission develops. Indeed, by plugging previous equations in the expression for the transmission and conductance, one ends up with the desired result that is plotted in Figs. 15, and 16.

In such plots, we consider a strong hopping t between sites in the leads in comparison to the couplings V and τ . For weak coupling between leads and the central region a resonant tunnelling peak is obtained at the energy of the central region $\omega = \varepsilon_d$. Upon increasing the coupling between the leads and the central region V the resonant peak at ε_d becomes broader and a sharp Fano feature emerges at the resonant impurity $\omega = \varepsilon_r$. The new feature has the typical Fano structure of a zero followed by

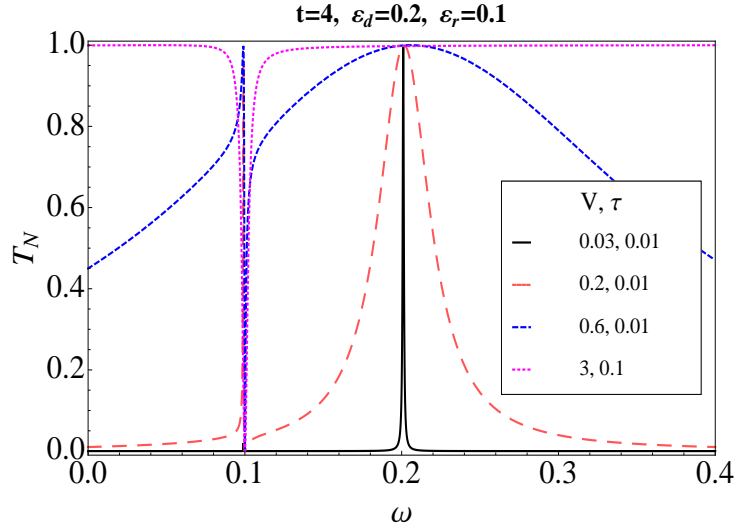


FIG. 15. (Color online) Normal transmission for the system described in this subsection B. Two tight binding semiinfinite chains (leads) coupled to central region formed by one site and where a resonant level is additionally weakly coupled to such central region. The hopping among sites in the leads is fixed and strong. By controlling the coupling to the leads V and the one to the resonant level τ one observes that the normal transmission exhibit a resonant peak at the energy of the quantum dot for weakly coupling, however, by making the coupling to the leads stronger and leaving weak the one to the resonant level, T_N develops a dip at the energy of the resonant level.

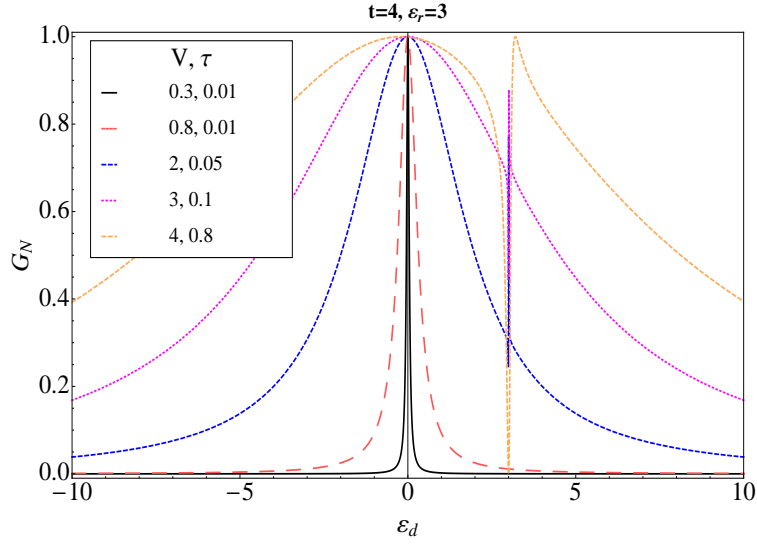


FIG. 16. (Color online) Normal conductance across a central region attached to two semiinfinite tight-binding chains (leads). In addition a resonant level is weakly coupled to such central region. The plots show the dependence of G_N on the energy of the quantum dot ε_d . The hopping among sites in the leads is fixed and strong. By controlling the coupling to the leads and the one to the resonant level one observes that the normal conductance exhibit a resonant peak when $\varepsilon_d = 0$, that is the Fermi energy of the leads $\omega_F = 0$, for weakly couplings, however, by making the coupling to the leads stronger and leaving weak the one to the resonant level, G_N develops a dip at the energy of the resonant level.

a peak, and arises from the interference of the two possible paths for the carriers, through the very broadened (strongly coupled) site at ε_d , and through the weakly coupled resonant level at ε_r . For strong enough coupling V , the ε_d contributes with a uniform e^2/h background to conductance, while the Fano feature becomes a pure dip

to zero.

In conclusion, we have developed an effective model that contains the physics involved in our numerics where a resonance peak is present at the energy of the quantum dot for weakly coupled system. By increasing the coupling of the quantum dot to the leads a Fano feature

(dip to zero followed by a peak) appears in conductance at the energy of the resonant level.

Appendix C: Majorana localization length

The calculation of ℓ_M is carried out by solving the polynomial equation for the wave vector k $k^2 + 4(\mu + C\alpha_R^2)Ck^2 + 8\lambda C^2\Delta\alpha_Rk + 4C_0C^2 = 0$, where $C = m/\hbar^2$ and $C_0 = \mu^2 + \Delta^2 - B^2$. Here, we point out that although the previous equation was derived in Ref. 20 for a semiinfinite case, it gives reasonable values for the Majorana localization length. Indeed, in Fig. 17 one observes that ℓ_M linearly increases as one increases B for realistic SOC (dashed line), while it acquires smaller values and remains roughly constant for stronger SOC (solid curve).

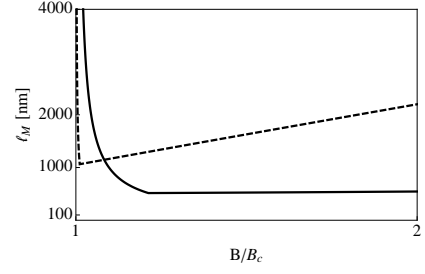


FIG. 17. Majorana localization length ℓ_M as a function of the Zeeman field B for $\alpha_R = \alpha_0$ (dashed curve) and $\alpha_R = 5\alpha_0$ (solid curve), where $\alpha_0 = 0.2\text{eV}\text{\AA}$. They correspond, to spin-orbit lengths $l_{SO} \approx 200\text{nm}$ and $l_{SO} \approx 40\text{nm}$, respectively. Rest of parameters $\mu = 0.5\text{meV}$, and $\Delta = 0.25\text{meV}$.